Impact of solute flow during directional solidification of a Ni-based alloy: In-situ and real-time X-radiography

G. Reinhart, D. Grange, L. Abou-Khalil, N. Mangelinck-Noel, N. T. Niane, V. Maguin, Gildas Guillemot, Ch.-A. Gandin, H. Nguyen-Thi

Impact of solute flow during directional solidification of a Ni-based alloy: in-situ and real-time X-radiography

G. Reinhart[a,*], D. Grange[b], L. Abou-Khalil[a], N. Mangelinck-Noël[a], N. T. Niane[b], V. Maguin[b,c], G. Guillemot[c], Ch.-A. Gandin[c], H. Nguyen-Thi[a]

[a] Aix Marseille Univ, Université de Toulon, CNRS, IM2NP, Marseille, France

[b] Safran Advanced Turbine Airfoils, a technology platform of Safran Tech, 171 Boulevard de Valmy, 92700 Colombes, France.

[c] PSL Research University, MINES ParisTech, CEMEF UMR CNRS 7635, CS10207, F-06904 Sophia Antipolis, France

Abstract

Understanding the impact of thermo-solutal convection during alloy solidification is of central importance in the casting industry. Convective flow generated from density variations in the liquid is at the origin of many casting defects, such as chemical segregations and freckles, to which Ni-based superalloys used in jet engines are known to be highly sensitive. In this article, we present experimental results obtained during directional solidification of a CMSX-4

[*] Corresponding author at Aix-Marseille University and IM2NP Case 142, Campus St-Jerome, 13397 Marseille cedex 20, France: Tel.: (+33) 4 91 28 28 94; Email address: guillaume.reinhart@im2np.fr

single crystal superalloy observed in-situ by means of synchrotron X-radiography at the European Synchrotron Radiation Facility (ESRF, Grenoble, France). The use of a high-temperature directional solidification furnace, an intense monochromatic beam and a high-speed X-ray sensitive camera allowed the direct observation of the development of solute flow to be performed during dendritic growth of a Ni-based alloy. The transient stage leading to the formation of a dendrite network and the interaction with the concomitantly developing convective pattern are studied. The impact of solute flow on the dendrite growth velocity is characterized for three cooling rates. Measurements of dendrite tip positions show that the convective flow above the solidification front induces a periodic oscillation of the dendrite growth velocity and that the oscillation amplitude decreases for higher cooling rates. The development of residual liquid areas is observed on the sides of the sample. Fragmentation of dendrite parts occurs during the solidification of the residual liquid areas and leads to the formation of spurious grains. The experimental results are analyzed by using a Rayleigh number-based model, highlighting the need for direct simulations in the future.

Keywords: Thermo-solutal convection; Superalloy; CMSX-4; Directional solidification; Synchrotron X-radiography

1. Introduction

Nickel-based superalloys are nowadays the reference material to produce blades for advanced turbine engines. Creep-resistant turbine blades and vanes are produced by lost-wax casting and directional solidification, enabling an accurate control of the microstructure and the manufacturing of single-crystal parts [1]. The need for higher turbine efficiency encourages the use of materials that are resistant to higher temperatures and stresses. Nevertheless, selecting materials with improved mechanical properties sometimes increases the challenges to process them. For instance, the widely used CMSX-4 single crystal superalloy is known to be sensitive to the occurrence of freckles, which are defects causing the affected parts to be rejected. Freckles appear as channels with a diameter proportional to few primary dendrite arm spacings. Their length can vary from millimeters to centimeters and they are filled with a chain of small equiaxed crystals [2]. In the case of a binary alloy with a partition coefficient less than unity and having a negative liquidus slope, freckles may be formed as follows. First, solute partitioning occurs at the scale of dendrite arms and solute is rejected in the melt, which intensifies the local composition gradients and results in an increase of the solutal buoyancy force. Then, segregation chimneys and convective plumes are formed, leading to partial melting of dendrites and eventually to the transport and accumulation of fragments and/or equiaxed crystals in the chimneys.

The understanding of freckle formation is difficult because it requires an accurate knowledge of local chemical segregation during solidification, as well as the prediction of liquid

density inversion and mushy zone permeability [3,4]. Because it is of prime importance to control the occurrence of freckles, several attempts have been made from the late 1960s [5] to the early 2000s [6] to understand and characterize it by deriving freckling criteria. These studies are summarized in [7]. It is possible to decrease or even suppress the occurrence of freckles by increasing the temperature gradient and/or the isotherm velocity during solidification [1,2], or by modifying the shape of the casting cluster. Simple predictors have been developed and are used in numerical simulation tools to evaluate the risk of defect occurrence. We can mention thermal based criteria and Rayleigh criteria: the thermal-based criteria use a combination of the temperature gradient G and the velocity of the isotherms V, while Rayleigh criteria includes the effect of alloy composition and mushy zone permeability [3,8]. However, too much constraint is put on the process at the expense of productivity when such criteria are not accurate enough. One of the limitations of those criteria is that the interaction between fluid flow due to thermo-solutal convection and the mold shape is not accurately considered. For example, it is well known that freckles can appear close to geometrical irregularities like section restrictions, due to a local concentration of the flow [9], a tendency that thermal-based and Rayleigh criteria fail to predict. Moreover, the internal surface of the mold (orientation, roughness…) do have effects that are also not considered [10]. Therefore, there is a major interest in developing multi-physical numerical simulations [11] that must be validated with accurate and relevant experimental observations [12].

In-situ observation is a valuable tool to improve the understanding of the solidification

processes [13], especially in the case of dynamical phenomena such as thermo-solutal flow occurring during alloy solidification. The pioneer studies using transparent alloys reported by Hellawell *et al.* [14] significantly pushed forward models of channel formation in the mushy zone. Over the last couple of decades, X-ray imaging has been established as the method of choice to carry out direct observations during the solidification of metal alloys [15]. Buoyancy-driven flow patterns have been studied in Ga-In alloys using X-ray radioscopy with a laboratory source by Boden *et al.* [16]. Their results have been particularly useful to make comparisons between experimental observations and numerical simulations of the formation of segregated channels [12] and freckles [17] and to investigate the impact of forced convection [18]. The study of alloys with a higher melting temperature such as aluminum-based alloy can also be carried out using laboratory devices that provide sufficient spatial and temporal resolutions to distinguish the growth microstructure [19–21]. To the best of the authors' knowledge, applications of these laboratory devices to the thorough investigation of flow patterns during solidification have not hitherto been reported. On the other hand, there now exists a significant body of works on the study of metallic alloy solidification using X-ray imaging at synchrotron source facilities by taking advantage of the high photon flux [22]. Among the various in-situ and time-resolved imaging techniques, such as synchrotron tomography [23–25] or Bragg diffraction imaging (also referred as X-ray topography) [26,27], synchrotron X-radiography is the simplest one to implement. Information on the composition variations in the liquid phase during binary metal alloys solidification can be retrieved from images by using synchrotron X-

radiography with a monochromatic X-ray beam [28,29] and to some extent three-dimensional spatial information [29,30]. The impact of thermo-solutal flow on the growth velocity of dendritic microstructures has been studied in Al-Cu-Si alloys by Mirihanage *et al.* [31] and in Sn-Pb alloys by Cao *et al.* [32]. Moreover, synchrotron imaging with high temperature furnaces makes it possible to study high temperature materials of industrial interest. Yasuda *et al.* [33] reported observations of the growth of δ-Fe dendrites by using synchrotron radiography. Tandjaoui *et al.* [34] combined synchrotron radiography and diffraction topography to study faceted silicon growth. First observations of dendrite growth and dendrite arm bending were reported in a Ni-based CMSX-4 superalloy by Aveson *et al.* [35,36]. It is worth noting that the dendritic pattern in Ni, Co and Fe-based alloys was recently observed by Azeem *et al.* by synchrotron tomography [37].

In this article, we present experimental results obtained during the directional solidification of a CMSX-4 single crystal superalloy observed in-situ and in real-time by means of synchrotron X-radiography at the European Synchrotron Radiation Facility (ESRF, Grenoble, France). The use of a high-temperature furnace, an intense monochromatic beam and a high-speed X-ray sensitive camera allowed us to carry out the direct observation of the development of solute flow during dendritic growth for a commercial CMSX-4 superalloy. The concomitant development of the dendrite network and of the convective pattern during the initial transient stage is described. The relative influence of solute flow on the dendrite development for three different cooling rates is highlighted. Observations of the development of residual liquid on the

sides of the sample as well as the formation of fragments and their movement in the residual liquid areas are described. Predictions of a Rayleigh number-based model adapted to each experimental case of interest are compared to the results. The advantages and limitations of such a model are discussed.

2. Experiments

2.1. Experimental procedure

Directional solidification experiments were carried out at the ID19 beamline of ESRF. The alloy samples were solidified/melted vertically inside the GaTSBI (Growth at high Temperature using a Synchrotron Beam for Imaging) experimental device schematized in Fig. 1a. This device was originally designed to study silicon growth and a detailed description of the equipment can be found elsewhere [38–40]. The sample was a single crystal of CMSX-4 alloy with a sheet-like shape. The nominal composition of the alloy is reported in Table 1 [41]. According to the Thermo-Calc NI25 database [42], the primary solid phase forming from the liquid state is disordered FCC with a liquidus temperature of 1384.2°C and a solidus temperature of 1317.6°C. Values of 1378.4°C for the liquidus temperature and of 1330.8°C for the solidus temperature were obtained using the Single Cristal database with the JMatPro® software [43].

The dimensions of the sample before melting was 43 mm × 7.8 mm × 0.3 mm. Photographs of the sample in its crucible before and after melting are shown in Fig. 1b. Shrinkage occurred

due to thickening of the sample after the first melting. The sample thickness was chosen to obtain enough transmission of the X-ray beam and to avoid the superimposing of several dendrite layers that would make the interpretation of the radiographs more difficult. The sample width was chosen to obtain a network composed of several dendrites. The single crystal orientation was chosen as shown by the reference frame displayed in Fig. 1b, i.e. with <100> crystallographic directions perpendicular to the sample faces. The sample was housed in a crucible made of dense alumina C799 (99.7 wt.% purity). It consisted of two plates maintained together by molybdenum clips with a 0.3 mm deep slot in one of the plates to accommodate the sample. The sample-crucible assembly was installed on a graphite holder connected to a graphite rod with a motorized translation device. The directional solidification furnace is composed of two heating zones made of graphite heaters that can reach up to 1800 °C in a secondary dynamical vacuum environment at a pressure around 10^{-4} mbar. The temperatures of the heating zones are regulated by two pyrometers with an accuracy of ± 0.1 °C. In the experiments described here, the temperature of the top "hot" zone was set to 1475 °C and the temperature of the bottom "cold" zone was set to 1255 °C, which corresponds to a temperature difference $\Delta T_{pyro} =$ 220 °C. The vertical distance between the two pyrometers was $\Delta z_{pyro} =$ 5 cm. The average longitudinal temperature gradient applied by the furnace was $G_F = \Delta T_{pyro}/\Delta z_{pyro} =$ 44 °C·cm^{-1}.

Melting/solidification cycles were applied to the sample while keeping constant the temperature gradient between the heaters. Upward directional solidification was triggered after

partial melting of the sample by decreasing the temperatures of the two heaters at the same cooling rate. The temperatures of both heaters were recorded during every cooling, stabilization and heating steps (Fig. 2). The temperature recordings were checked after the experiments and no fluctuations above the accuracy of the pyrometers were noticed. The cooling rate values considered in the present study are $R_1 = -2$ °C·min^{-1}, $R_2 = -4$ °C·min^{-1} and $R_3 = -8.3$ °C·min^{-1}.

Synchrotron X-radiography was used to visualize in-situ and in real-time the evolution of the solidification front. The X-ray beam energy was set to 40 keV using a double Si(111) monochromator. This energy value ensured enough transmission of the X-rays through the sample, as well as a satisfactory contrast between the solid and liquid phases. Radiographs were recorded on a sCMOS pco.edge 5.5 camera [44]. The optics were chosen to provide a pixel size of 6.6 µm × 6.6 µm and a field of view of 9.9 mm × 9.9 mm (Fig. 1a). The time intervals between two successive images were 0.1, 0.25 and 0.5 seconds for the cooling rates of –8.3, –4 and –2 °C·min^{-1}, respectively. It is worth noting that the distance between the sample and the camera was approximately 8 meters. This large distance induced phase contrast in the images [45], especially at the edges between the solid and the liquid regions. Phase contrast was used to facilitate the visualization of the microstructure, since previous investigations have shown that a low absorption contrast is expected for this alloy [35,36].

2.2. Image processing

The legibility of the raw images is made difficult by several spurious artefacts and required the application of image processing procedures as illustrated in Fig. 3. Among the artefacts, one can mention the variation of the X-ray beam intensity profile in time and space, and the surface defects of the silicon crystals of the monochromator (Fig. 3a). A common image processing used to remove these artefacts is to apply a flat-field correction using a reference image recorded just before applying the cooling rate [28]. This procedure was not successful in correcting the radiographs in a satisfactory manner because the graphite rod used to insert the sample in the furnace was contracting during the temperature decrease. This contraction induced a slight and gradual upward motion of the sample in the field of view that reached approximately 60 µm during a whole solidification experiment. The resulting misalignment between the images of the sample during cooling and the reference image used for the flat-field correction lead to a detrimental decrease of the image legibility.

Two complementary procedures were devised with the image processing software ImageJ [46]. In the first process, the images of the sample were aligned to compensate for the upward motion. The best results were obtained using the TurboReg plugin for ImageJ, which is a sub-pixel registration algorithm developed by Thévenaz *et al.* [47]. Then, a flat-field correction was applied with a reference image recorded just before applying the cooling rate (Fig. 3b). The resulting images clearly displayed the growth microstructure but also additional striated

contrasts (horizontal black and white lines) corresponding to monochromator defects that were no longer properly corrected (Fig. 3c).

The aligned images were also used for the second process and a frame differencing procedure was applied. Frame differencing is a well-known technique used in computer vision where the computer enlightens the differences between two video frames, for example to highlight movements. In the present case, it was possible to reveal changes in the solidification microstructure by dividing (or subtracting) an image by a previous one [48] (Fig. 3d). The offset between the two images was chosen so that the amount of solid that was formed during the time interval was clearly distinguished in the top part of the mushy zone (black dendritic structures Fig. 3e). An overlay of the current and previous microstructures is also visible in the bottom part. With this second image processing, gray-level variations in the liquid phase became visible as shown by the white arrows in Fig. 3e. These gray-level variations correspond to changes in composition due to solute rejection. Hence, the visualization of solutal convective flow ahead of the dendrite network was made possible. To summarize, the frame differencing procedure implemented with the ImageJ software [46] consisted of the following steps:

- Aligning all raw images with the first image by using the TurboReg plugin [47].
- Differencing successive frames with a constant offset.
- Choosing the offset so that the features of interest do not superimpose on the resulting images.

Despite the difficulty in interpreting the images obtained by frame differencing, the visualization of convective flow and the correction of the monochromator defects make it a

valuable procedure to study the solidification of materials having a low absorption contrast between their constitutive elements.

3. Results

3.1. Onset of thermo-solutal flow

An initially still solid-liquid interface was positioned at the bottom of the field of view by partially melting the sample from the top and then by stabilizing for approximately 2 hours between each experiment (Fig. 2). We will first focus on the experiment performed with a cooling rate $R_1 = -2$ °C·min^{-1} and for which the influence of convective flow on the growth process was the most noticeable (Supplementary Movie 1). The initial solid-liquid interface is shown on a raw image in Fig. 4a. The top part of the sample is fully liquid, and the bottom part is fully solid due to the migration of the solute-rich liquid regions toward the top of the mushy zone by Temperature Gradient Zone Melting (TGZM) as described by Nguyen-Thi *et al.* [48,49]. The solid phase appears darker than the liquid phase and the interface is slightly convex. The curvature of the solid-liquid interface was observed for each experiment. It is caused by a transversal temperature gradient G_y from the center to the side of the sample, due to the complex radiative heat transfer between the furnace and the crucible as well as the different thermal properties of the liquid, the solid and the crucible. A rough estimation of G_y can be made by using the procedure proposed by Bogno *et al.* [50] in a study of a binary Al-Cu alloy by X-radiography. The transversal temperature gradient was calculated using $G_y =$

$(h/d)\ G_F$ with h the distance between the highest and lowest levels of the curved front and d the corresponding transversal distance. By this means, it was deduced that the transversal temperature gradient was of the order of 3 °C·cm^{-1} toward the left and 5 °C·cm^{-1} toward the right. These values are much lower than the applied longitudinal temperature gradient $G_F =$ 44 °C·cm^{-1}.

Solidification was visible shortly after application of the cooling rate. Growth was detected by the development of a dark layer (Fig. 4b) corresponding to an initial phase of planar growth without microstructure formation. The striations at larger distances are surface defects from the silicon crystals of the monochromator that could not be totally corrected due to a technical glitch that induced a sudden variation of the monochromator position. The light-gray layer above the growth interface shown in Fig. 4b and measured in Fig. 4c corresponds to the rejection of light solute elements during solidification. The rejection of light solute elements reduces the liquid density and consequently the X-ray absorption. The build-up of the solutal layer lasted for about 150 seconds and small cellular structures developed with a primary spacing of approximately 50 µm. Then, the solutal layer destabilized to form 4 solute plumes (Fig. 4d) with a maximum height ranging from 1 to 2 mm before vanishing. The low gray level dynamic and important noise in the images prevented preliminary attempts to use optical flow approaches as carried out by Boden *et al.* [16]. However, a rough estimation of the ascending velocity was obtained by manually measuring the displacement of contour lines defined for a given brightness between two positions of the plumes. Measurements gave velocity values of

the order of 25 to 35 $\mu m \cdot s^{-1}$ with an error of ± 0.6 µm/s. It is worth noting that the solute plumes were moving upward but also slightly toward the left. Growth was inhibited in the areas just below the plumes due to the local accumulation of solute, as shown by the white arrows numbered 1 to 4 in Fig. 4d.

Columnar dendritic microstructures were well developed after approximately 200 s (Fig. 5a) and the solute plumes were not visible anymore. The solidification front exhibited no-dendrite regions, as shown by the dashed white arrows in Fig. 5a, where the plumes were previously observed (Fig.4d). Later, new plumes developed above the already well-developed dendrites (plain arrows in Fig. 5b). The plumes overtook the dendrites because their ascending velocity was higher than the dendrite growth velocity. The local accumulation of solute slowed the growth of the well-developed dendrites and the previously lagging structures caught up with the top of the solidification front.

The columnar dendrites kept on developing by successive deceleration and acceleration periods correlated with the formation of plumes but also with the lateral drift of the plumes from right to left (Fig. 5c). This drift velocity was measured manually and was of the order of 10 $\mu m \cdot s^{-1}$ to 20 $\mu m \cdot s^{-1}$ with an error of ± 0.6 µm/s. Concomitantly, a long solute plume developed on the left side of the sample (vertical white arrow in Fig.5c and in Fig. 5d), indicating that a large convective loop was formed in the sample.

When the solidification front reached the top of the field of view, the growth pattern was composed of a columnar dendrite network with continuous formation of solute plumes drifting

toward the left side of the sample, where a vertical segregated channel was formed. It is worth noting that a vertical channel was also formed on the right-hand side, but much thinner.

The same sequence was observed during the experiment with the cooling rate $R_2 = -4$ °C·min^{-1} leading to a similar growth pattern as can be seen on Supplementary Movie 2, except that the first plumes appeared when the interface was already destabilized, the plume height was smaller (about 0.5 mm) with a slower drift velocity (about 5 to 10 µm·s^{-1}), and thin vertical channels were formed on both sides of the sample. For the highest cooling rate $R_3 = -8.3$ °C·min^{-1}, no solute plumes were observed above the solidification front, and only thin vertical channels developed on the sides of the sample as can be seen on Supplementary Movie 3.

3.2. Influence of cooling rate on dendrite growth

The growth microstructure when the solidification front reached approximately two thirds of the field of view is shown in Fig. 6 for the three cooling rates. An average primary spacing $\lambda_1 =$ 330 µm, 317 µm and 290 µm was measured for the cooling rates $R_1 = -2$ °C·min^{-1}, $R_2 = -4$ °C·min^{-1} and $R_3 = -8.3$ °C·min^{-1}, respectively. The dendrites on the left side and on the right-hand side of the sample have different morphologies, which means that the sample is made of two slightly misoriented sub-grains although a single crystal sample was originally targeted. Measurement of the misorientation between the growth directions of the grains gave a value of about 7°. A similar misorientation value was obtained by post-mortem EBSD (Electron BackScatter Diffraction) analysis. The corresponding pole figures of both grains are

shown in Fig. 6c. The different growth orientation of the dendrites was therefore due to the different crystallographic orientation of the sub-grains with respect to the temperature gradient direction.

The position of a central dendrite tip (white arrows in Fig. 6) was measured as a function of time for each experiment (Fig. 7, first row). The error on the position depends on the pixel size and was ± 6.6 µm. The growth velocities were calculated from the tip positions (Fig.7, second row) with a systematic error of ± 0.6 µm/s. Average gray values were also measured in a 130 µm by 130 µm square box, centered 130 µm above the tip (Fig.7, third row). The brightness could not be directly converted into concentration values by using an adapted Beer-Lambert law [28,29] because a monochromatic beam was used to visualize a multi-component alloy. However, gray-level variations in the liquid phase were representative of the change in density and composition. A brightness increase corresponds to an enrichment of the liquid in light solute elements, allowing a qualitative interpretation of the impact of solute concentration variations on the dendrite growth kinetic.

It is visible in Fig. 7 that solute flow has a significant impact on dendrite growth for the cooling rates $R_1 = -2$ °C·min^{-1} and $R_2 = -4$ °C·min^{-1}. In both experiments, the dendrite tip did not move regularly upward in the field of view, but successively moved upward and then remained almost still. This trend was evidenced by periodic oscillations in the velocity plots. The mean period was around 80 seconds for the velocity R_1, with growth velocity values oscillating between 25 µm·s^{-1} and 0.5 µm·s^{-1} and an average growth velocity $\langle V_1 \rangle$ = 7.6 µm·s^{-}

[1]. The oscillation in growth velocity was also observed for the cooling rate $R_2 = -4$ °C·min^{-1} (Fig. 7b). The growth velocity oscillated around an average value $\langle V_2 \rangle$ = 15 µm·s^{-1} but the oscillations were progressively damped. Here, the solidification front left the field of view before a permanent regime was reached. So, it was not possible to determine if the oscillating regime would have continued or if the solidification front would have reached a constant growth velocity after a transient stage. The oscillations of the growth velocity were directly correlated with the gray level variations. The maxima of gray level coincided with the minima of growth velocity and vice-versa. The gray level variations corresponded to composition variations above the dendrite tip due to solute flow. So, an increase (resp. decrease) in solute concentration ahead of the dendrite tip coincided with a decrease (resp. increase) of the growth velocity.

The growth velocity for the cooling rate $R_3 = -8.3$ °C·min^{-1} reached an average value $\langle V_3 \rangle$ = 31 µm·s^{-1} after a single period of acceleration and deceleration (Fig. 7c), typical of an overdamped regime. The gray level above the tip rapidly decreased to reach a constant value, indicating that the composition ahead of the tip remained constant after the transient stage.

Finally, the temperature gradients at the level of the dendrite tips was estimated by using the relation $\langle G_{tip} \rangle = R/\langle V_{tip} \rangle$ with $\langle V_{tip} \rangle$ the average growth velocity of a dendrite tip. Temperature gradient values $\langle G_1 \rangle$= 44 °C·cm^{-1}, $\langle G_2 \rangle$=44.5 °C·cm^{-1}and $\langle G_3 \rangle$= 45 °C·cm^{-1} were obtained. These close values sustain the fair comparison of the experiments. It is worth noting that they are also close to the average temperature gradient applied by the furnace G_F = 44 °C·cm^{-1}. Further investigations using numerical models are in progress to improve the

understanding of the thermal behavior of the experimental device and will be the subject of future publications.

3.3. Solidification of residual liquid areas

Solute flow developed above the solidification front for the two experiments with the slowest cooling rates. However, vertical liquid channels were formed along the edges of the sample even for the fastest cooling rate. A consequence of the liquid channel formation was the development of residual liquid areas as indicated by the red circles in Fig. 8. The origin of the residual liquid areas was the local accumulation of solute leading to the dissolution of the microstructure. The enriched liquid had a lower solidification temperature, and consequently the residual liquid areas solidified later during the cooling stage.

A sequence of images recorded during the solidification of the liquid area observed on the left side of the sample during the cooling rate $R_1 = -2$ °C·min^{-1} is shown in Fig. 9. The liquid area reached a maximum width and height of approximately 0.65 mm and 2.5 mm, respectively. With time, the microstructure started to slowly protrude in the liquid, as shown in the image obtained by frame differencing (Fig. 9b). A small equiaxed dendrite was observed during its fall from the top of the liquid area (white arrow in Fig. 9b). It was not possible to determine with the current temporal resolution whether the grain nucleated in the liquid phase or originated from the fragmentation of a columnar dendrite. Then, horizontal dendritic microstructures grew, and dendrite fragmentations were clearly detected. Unexpectedly, some

fragments moved upward (Fig. 9c) and others settled down (Fig 9d) within an interval of a few seconds. The residual liquid area was eventually filled with small misoriented grains and a segregated zone was formed next to it, extending diagonally from the middle of the sample toward the top left of the field of view as can be seen on Supplementary Movie 4 and above the white arrow in Fig. 9e.

4. Discussion

4.1. Solute plume formation and evolution

The use of synchrotron radiography allowed the visualization of solute plumes to be performed during the directional solidification of a Ni-based alloy. The first solute plumes developed because the solutal layer above the solid-liquid interface was inherently unstable. Solute rejected during solidification formed a layer of light liquid located below a heavier bulk liquid at nominal composition. The liquid layer destabilization occurred when the buoyancy force due to the density inversion overcame the fluid inertia, which is limited by the viscosity and the thermal conductivity of the liquid, as previously explained by Hellawell *et al.* [14] or Nguyen-Thi *et al.* [51].

Another experimental observation is that the first solute plumes moved upward but also slightly toward the left side of the sample. On first analysis, this plume drift could be due to convective flow already present in the vicinity of the solid-liquid interface. The transversal temperature gradient gives rise to a curvature of the solid-liquid interface (Fig.4a) , which can induce a weak convective flow from the highest position of the interface toward the sides of the

sample although not detectable by gray-level variations in the liquid phase [50,52]. However, such a flow would push the plumes in a direction opposite to the observation (i.e. from the center to the side, while the plumes are moving from the side toward the center). The origin of the plume lateral drift can thus be attributed to the fact that the first and largest plume formed at the highest position of the solid-liquid interface, which was located slightly on the left side of the sample. This symmetry breaking initiated the development of a convective loop moving from the right to the left side, eventually leading to the formation of the liquid channel on the left side of the mushy zone.

4.2. Effect of solute flow on dendrite growth

As reported in section 3.2, the measured primary spacing λ_1 decreased from 330 µm to 317 µm and 290 µm when increasing the cooling rate or, equivalently, when increasing the growth velocity. The relation $\lambda_1(\mu\mathrm{m}) = 147\ (G\,V)^{-0.3384}$ has been proposed by Bouse and Mihalisin [53] to predict the primary spacing in Ni-based superalloys and was found to be applicable to a wide range of superalloys, temperature gradients and solidification velocities. This relation was also used in numerical simulations investigating the conditions for the formation of freckle defects [6,8,54]. The calculated values for growth velocities of 7.5, 15 and 31 µm·s^{-1} are 464 µm, 367 µm and 287 µm, respectively. Recently, Matache *et al*. [55] directly measured the evolution of the primary spacing in CMSX-4 superalloy and deduced the relation $\lambda_1(\mu m) = 1865\ V^{-0.25} G^{-0.5}$ that is appropriate for comparison with directional solidification

experiments. The calculated values with this relation and for growth velocities of 7.5, 15 and 31 $\mu m \cdot s^{-1}$ are 537 µm, 452 µm and 377 µm, respectively. A good agreement is obtained for the fastest velocity and significantly higher values are predicted for the two other velocities.

The calculated values were determined from bulk sample analyses and the discrepancy between the calculated and measured values occurs when the primary spacing is larger than the sample thickness. This suggests that the microstructure confinement would decrease the primary spacing. Recent numerical simulations carried out by Tourret *et al.* [56] using the Dendrite Needle Network (DNN) model compared directional solidification of dendritic networks in 2D and 3D configurations. The results showed that a higher primary spacing is in fact expected for confined configurations in diffusive regime. So, another explanation is necessary to explain the discrepancy between calculated and experimental values of primary spacing. As the discrepancy is only observed for the two slowest growth rates, when solute plumes above the solidification front were visible, it can be attributed to the impact of solute flow ahead of the dendrite network. The same effect, namely smaller primary spacings compared to diffusive theories at low growth velocity and with convective flow above the solidification front, was also reported by Clarke *et al.* [57] and Yang *et al.* [58] and is linked to modifications of the solute field in the solutal layer above the dendrite network by convective flow.

Concerning the oscillations of the dendrite growth velocity due to solute plume development as reported in section 3.2 (Fig. 7), the same behavior was reported by Boden *et al.*

in Ga-In alloys [16], Mirihanage *et al.* in Al-Cu-Si alloys [29], Cao *et al.* [32] in Sn-Pb alloys. It was also recently analyzed numerically for superalloy directional solidification by Yang *et al.* [58]. The increase in solute concentration above the dendrite tips was due to solute rejection during solidification. Light solute elements flowed upward faster than the dendrites developed, and the concentration gradient above the dendrite tips decreased. Consequently, the growth velocity decreased because the concentration gradient above the dendrite tips is the driving force for growth during directional solidification. In a similar way, the concentration gradient increased after dissipation of the solute plume, increasing the growth velocity. After the early stage of growth, the variations in solute concentration above the dendrite tips were linked to the lateral drift of the plumes, with the solute concentration increases and the concentration gradient decreases above the tips following the arrival of a plume.

The oscillation damping for the cooling rate $R_2 = -4$ °C·min^{-1} indicates that convective flow had less impact on the dendrite growth. It is also worth noting that the initial variation in growth velocity for the fastest cooling rate $R_3 = -8.3$ °C·min^{-1} is not related to the formation of solute plumes since none were observed, but as a matter of fact corresponds to the initial transient of solidification as described by Warren and Langer [59] for diffusive conditions. The solidification front had to temporarily grow at a higher velocity to catch up the time necessary to build-up a solutal layer from an initially still interface. This is also an indication that solute flow did not have time to develop above the solidification front for this cooling rate.

4.3. Impact of fluid flow in the mushy zone

The main results of the present experiments are the observation of solute plumes, their interaction with the columnar dendrites and the formation of residual liquid areas and liquid channels. These observations suggest that one possible scenario for the formation of spurious grains, and possibly freckles, is the formation of residual liquid areas on the sample edges and their subsequent solidification. The latter involves growth of dendrite arms located at the periphery of the residual liquid areas and their fragmentation due to thermo-solutal convection. The fragments are transported and can grow, eventually leading to an equiaxed grain structure.

The formation of plumes and liquid channels is due to the interaction of buoyancy and frictional forces in the liquid. Thus, in a first approach , the Rayleigh number Ra that is defined as the ratio of the driving buoyancy force to the retarding frictional force associated with the permeability of the mush is the dimensionless parameter of choice to characterize these phenomena [6]. The Rayleigh number in the mushy-zone was calculated based on the definition proposed by Beckermann *et al.* [8]:

$$Ra(h) = [(g\,\overline{K}(h)\,h)/(\alpha v)]\left[(\rho_L^l - \rho^l(h))/\rho_L^l\right] \quad (1)$$

It is written for a given depth in the mushy zone h. The constants g, α and v represents the gravitational constant (equal to $9.81\ \mathrm{m \cdot s^{-2}}$), the thermal diffusivity and the kinematic viscosity, respectively. The αv value was $6 \cdot 10^{-12}\ \mathrm{m^4 \cdot s^{-2}}$ for the nominal composition

and the liquidus temperature obtained using the Single Cristal database of JMatPro® software [43]. This value is close to the value found in reference [8] (i.e., $5 \cdot 10^{-12}\ \mathrm{m}^4 \cdot \mathrm{s}^{-2}$).

Assuming that the longitudinal temperature gradient G_z is constant in the mushy zone, the local temperature T is computed using the relation $T = T_L - G_z\, h$ where T_L is the liquidus temperature of the alloy. The relative density of the liquid phase is computed with the ratio:

$$(\rho_L^l - \rho^l(h))/\rho_L^l \tag{2}$$

where ρ_L^l and $\rho^l(h)$ are the liquid densities at T_L and at the local temperature T, respectively. The mean permeability $\overline{K}(h)$ is computed with the relation:

$$\overline{K}(h) = K_0 \left(1 - \overline{\varepsilon^s}(h)\right)^3 / \overline{\varepsilon^s}(h)^2 \tag{3}$$

where $K_0(m^2) = 6 \cdot 10^{-4}\ \lambda_1^2$ is deduced by correlation with experimental observations in several nickel base superalloys. Note that the primary spacing only plays a role in computing the permeability in the present analyses. The experimental primary dendrite arm spacing values λ_1 are used and are reported section 3.2. The average volumetric solid fraction $\overline{\varepsilon^s}(h)$ is evaluated by:

$$\overline{\varepsilon^s}(h) = \frac{1}{h}\int_0^h \varepsilon^s(y)dy \tag{4}$$

where $\varepsilon^s(y)$ is the solid fraction associated to a depth y in the mushy zone. The solidification path and the liquid density evolution need to be computed. This is done using the thermodynamic database NI25 provided by ThermoCalc [42] and the Single Cristal database of JMatPro® software [43], with the Lever-rule and Gulliver-Scheil hypotheses.

The influence of the thermodynamic databases on the Rayleigh number is presented in Fig. 10a for a cooling rate R_1 = –2 °C·min^{-1}. The plain red and black curves are obtained using the Lever-rule solidification path with the NI25 and the Single Cristal databases, respectively. The dashed red and black curves are obtained using the Gulliver-Scheil solidification path with the NI25 and the Single Cristal databases, respectively. The differences between the curves come from the very different liquidus and solidus temperatures that are considered, as well as the solidification path computed from the databases. The main feature to notice is the temperature range below the liquidus temperature where positive values of the *Ra* number are obtained due to liquid density inversion, i.e. positive ratio $(\rho_L^l - \rho^l(h))/\rho_L^l$. For every case, the *Ra* number values increase very rapidly just below the liquidus temperature. This indicate that solute rejection of light elements close to the solidification front is the driving force for the formation of solute plumes and to sustain their development as experimentally observed.

The maximum of the *Ra* curves is higher with the Gulliver-Scheil model and more marked for the Single Cristal database. For the same cooling conditions and with the Gulliver-Scheil micro-segregation model, the *Ra* reaches a maximum value of 5.9·10^{-3} for the NI25 database

and of $1.8 \cdot 10^{-2}$ for the Single Cristal database. Although, these values are much smaller than the threshold value of 0.25 proposed in the literature for the occurrence of segregated channels [8], the development of a diagonal segregated channel was nevertheless observed experimentally in the mushy zone (Fig. 9 and Supplementary Movie 3).

The NI25 database predicts a positive *Ra* for a temperature range of 6 °C below the liquidus temperature using the Lever-rule and 12 °C using Gulliver-Scheil, whereas the Single Cristal database a temperature range of 22 °C using the Lever-rule and of 47 °C using Gulliver-Scheil. In the experiments with a cooling rate $R_1 = -2$ °C·min^{-1}, the diagonal segregated channel formed approximately 20 minutes after the solidification front crossed the same position. Assuming that the columnar dendrites are growing at a temperature close to the liquidus temperature, it can be deduced that the segregated channel was formed 40 °C below the liquidus temperature. Since a positive *Ra* number is necessary for fluid flow to occur, the calculation using the Single Cristal database and the Gulliver-Scheil solidification path are therefore in better agreement with the experimental observation.

Because the temperature gradient is constant for these experiments, the increase of the cooling rate decreases the primary dendrite arm spacing and the associated mean permeability. Consequently, the Rayleigh number also decreases when increasing the cooling rate (Fig. 10b). The present in-situ observations also showed a lower macro-segregation activity for the highest cooling rates, with the formation of much smaller liquid areas and no segregated channel.

The accurate location of the residual liquid areas and segregated channel is currently

difficult to predict without direct simulation of solute flow in the mushy zone. The deformation of the sample sides, even small, could also impact the solute flow and lead to local segregation areas. More advanced and direct simulations are therefore necessary to improve the understanding of how the solid fraction increase in the mushy zone interrupted the solute feeding of the residual liquid areas, leading to their solidification. Such a phenomenon is also currently hard to characterize using the present radiography data.

Finally, the fact that dendrites appear darker than the surrounding liquid indicates that they are denser, which agrees with the downward motion of fragments. However, the concomitant upward motion of dendrite parts suggests that significant fluid flow developed in the residual liquid area while solidifying, with enough intensity to transport the fragments. Again, simulations of the present solidification process providing they consider the impact of fluid flow may help to propose a more detailed analysis of the origin of such phenomena in the future.

5. Conclusion

The directional solidification of a CMSX-4 single crystal superalloy was studied in-situ by synchrotron X-radiography using a high-temperature directional solidification furnace. The development of solutal flow ahead of the solidification front was directly observed. The initial stage of solidification was analyzed, and the onset of the convective pattern was described for different cooling rates. Solute plumes formed above the solidification front at slow growth rates and liquid channels formed on the sides of the sample for every investigated cooling rates. The

impact of solute flow was quantitatively characterized by measuring the position and velocity of dendrites located at the center of the sample. A periodic oscillation of the growth velocity was observed at slow growth rate, which did not occur for the fastest growth rate. This behavior was correlated with the development of solute plumes for the various applied cooling rates. The formation and solidification of residual liquid areas on the sides of the sample was reported. Various motions of fragments were observed inside the residual liquid area indicating that solute flow from the surrounding mushy region played a role in the formation of spurious grains and possibly in channels of equiaxed grains forming the freckle defect.

It was also determined that, despite the inherent merits of a Rayleigh number criterion to evaluate the formation of segregated channels, its calibration highly depends on the material and on the thermodynamic properties. Effect of thermodynamic databases was shown, and the maximum value computed for the Rayleigh number remains very low compared to the critical value reported in the literature. Among other limitations, a criterion based on the Rayleigh number can only hardly be extended to account for complicated geometries and non-directional heat flow. Direct numerical simulations are to be targeted to get a better understanding of the effect of the fluid flow on the structure and segregation patterns, to predict the location of residual liquid area formation, segregation channels and, possibly, freckles. The challenge not only lies in coupling three-dimensional thermo-hydraulic and thermo-solutal simulations with microstructure formation, but also multicomponent solidification paths with thermodynamic databases. Furthermore, coupling needs to be achieved while simulating the entire directional

solidification process as heat and mass transfers are highly dependent on time evolving boundary conditions. Achieving complementary in-situ observations would certainly be invaluable for the validation of such direct numerical simulations.

Acknowledgements

This study was funded by SAFRAN Tech (Gennevilliers, France). The financial support of the French National Space Agency (CNES) and the technical support from the ESRF (Grenoble, France) members E. Boller, V. Fernandez, A. Rack, and J. P. Valade is also acknowledged.

Appendix A. Supplementary data

Supplementary data related to this article can be found at (link to supplementary material)

References

[1] T.M. Pollock, S. Tin, Nickel-Based Superalloys for Advanced Turbine Engines: Chemistry, Microstructure and Properties, J. Propuls. Power. 22 (2006) 361–374. https://doi.org/10.2514/1.18239.

[2] S.M. Copley, A.F. Giamei, S.M. Johnson, M.F. Hornbecker, The origin of freckles in unidirectionally solidified castings, Metall. Trans. 1 (1970) 2193–2204. https://doi.org/10.1007/BF02643435.

[3] P. Auburtin, S.L. Cockcroft, A. Mitchell, Liquid Density Inversions During the Solidification of Superalloys and Their Relationship to Freckle Formation in Castings, in: Superalloys 1996 Eighth Int. Symp., TMS, 1996: pp. 443–450. https://doi.org/10.7449/1996/Superalloys_1996_443_450.

[4] J.A. Dantzig, M. Rappaz, Solidification: Methods, Microstructure and Modelling, EPFL Press, 2009.

[5] R. Mehrabian, M. Keane, M.C. Flemings, Interdendritic fluid flow and macrosegregation; influence of gravity, Metall. Mater. Trans. B. 1 (1970) 1209–1220. https://doi.org/10.1007/BF02900233.

[6] J.C. Ramirez, C. Beckermann, Evaluation of a rayleigh-number-based freckle criterion for Pb-Sn alloys and Ni-base superalloys, Metall. Mater. Trans. A. 34 (2003) 1525–1536. https://doi.org/10.1007/s11661-003-0264-0.
[7] P.B.L. Auburtin, Determination of the influence of growth front angle on freckle formation in superalloys, University of British Columbia, 1998.
[8] C. Beckermann, J.P. Gu, W.J. Boettinger, Development of a freckle predictor via rayleigh number method for single-crystal nickel-base superalloy castings, Metall. Mater. Trans. A. 31 (2000) 2545–2557. https://doi.org/10.1007/s11661-000-0199-7.
[9] D. Ma, A. Bührig-Polaczek, The Geometrical Effect on Freckle Formation in the Directionally Solidified Superalloy CMSX-4, Metall. Mater. Trans. A. 45 (2014) 1435–1444. https://doi.org/10.1007/s11661-013-2088-x.
[10] D. Ma, A. Bührig-Polaczek, The Influence of Surface Roughness on Freckle Formation in Directionally Solidified Superalloy Samples, Metall. Mater. Trans. B. 43 (2012) 671–677. https://doi.org/10.1007/s11663-012-9691-x.
[11] A. Saad, C.-A. Gandin, M. Bellet, Temperature-based energy solver coupled with tabulated thermodynamic properties – Application to the prediction of macrosegregation in multicomponent alloys, Comput. Mater. Sci. 99 (2015) 221–231. https://doi.org/10.1016/j.commatsci.2014.12.009.
[12] A. Saad, C.-A. Gandin, M. Bellet, N. Shevchenko, S. Eckert, Simulation of Channel Segregation During Directional Solidification of In—75 wt pct Ga. Qualitative Comparison with In Situ Observations, Metall. Mater. Trans. A. 46 (2015) 4886–4897. https://doi.org/10.1007/s11661-015-2963-8.
[13] S. Akamatsu, H. Nguyen-Thi, In situ observation of solidification patterns in diffusive conditions, Acta Mater. 108 (2016) 325–346. https://doi.org/10.1016/j.actamat.2016.01.024.
[14] A. Hellawell, J.R. Sarazin, R.S. Steube, Channel convection in partly solidified systems, Philos. Trans. R. Soc. Lond. Ser. Phys. Eng. Sci. 345 (1993) 507–544. https://doi.org/10.1098/rsta.1993.0143.
[15] H. Nguyen-Thi, L. Salvo, R.H. Mathiesen, L. Arnberg, B. Billia, M. Suery, G. Reinhart, On the interest of synchrotron X-ray imaging for the study of solidification in metallic alloys, Comptes Rendus Phys. 13 (2012) 237–245. https://doi.org/10.1016/j.crhy.2011.11.010.
[16] S. Boden, S. Eckert, B. Willers, G. Gerbeth, X-Ray Radioscopic Visualization of the Solutal Convection during Solidification of a Ga-30 Wt Pct In Alloy, Metall. Mater. Trans. A. 39 (2008) 613–623. https://doi.org/10.1007/s11661-007-9462-5.
[17] S. Karagadde, L. Yuan, N. Shevchenko, S. Eckert, P.D. Lee, 3-D microstructural model of freckle formation validated using in situ experiments, Acta Mater. 79 (2014) 168–180. https://doi.org/10.1016/j.actamat.2014.07.002.
[18] N. Shevchenko, O. Roshchupkina, O. Sokolova, S. Eckert, The effect of natural and forced melt convection on dendritic solidification in Ga–In alloys, J. Cryst. Growth. 417 (2015)

1–8. https://doi.org/10.1016/j.jcrysgro.2014.11.043.
[19] H. Nguyen-Thi, G. Reinhart, G. Salloum Abou Jaoude, R.H. Mathiesen, G. Zimmermann, Y. Houltz, D. Voss, A. Verga, D.J. Browne, A.G. Murphy, XRMON-GF: A novel facility for solidification of metallic alloys with in situ and time-resolved X-ray radiographic characterization in microgravity conditions, J. Cryst. Growth. 374 (2013) 23–30. https://doi.org/10.1016/j.jcrysgro.2013.03.032.
[20] A.G. Murphy, R.H. Mathiesen, Y. Houltz, J. Li, C. Lockowandt, K. Henriksson, G. Zimmermann, N. Melville, D.J. Browne, XRMON-SOL: Isothermal equiaxed solidification of a grain refined Al–20 wt%Cu alloy, J. Cryst. Growth. 440 (2016) 38–46. https://doi.org/10.1016/j.jcrysgro.2016.01.032.
[21] M. Becker, S. Klein, F. Kargl, In-situ solute measurements with a laboratory polychromatic microfocus X-ray source during equiaxed solidification of an Al-Ge alloy, Scr. Mater. 124 (2016) 34–37. https://doi.org/10.1016/j.scriptamat.2016.06.032.
[22] A.J. Clarke, D. Tourret, S.D. Imhoff, P.J. Gibbs, K. Fezzaa, J.C. Cooley, W.-K. Lee, A. Deriy, B.M. Patterson, P.A. Papin, K.D. Clarke, R.D. Field, J.L. Smith, X-ray Imaging and Controlled Solidification of Al-Cu Alloys Toward Microstructures by Design, Adv. Eng. Mater. 17 (2015) 454–459. https://doi.org/10.1002/adem.201400469.
[23] O. Ludwig, M. Dimichiel, L. Salvo, M. Suéry, P. Falus, In-situ three-dimensional microstructural investigation of solidification of an Al-Cu alloy by ultrafast x-ray microtomography, Metall. Mater. Trans. A. 36 (2005) 1515–1523. https://doi.org/10.1007/s11661-005-0243-8.
[24] J.W. Gibbs, K.A. Mohan, E.B. Gulsoy, A.J. Shahani, X. Xiao, C.A. Bouman, M. De Graef, P.W. Voorhees, The Three-Dimensional Morphology of Growing Dendrites, Sci. Rep. 5 (2015) 11824. https://doi.org/10.1038/srep11824.
[25] B. Cai, J. Wang, A. Kao, K. Pericleous, A.B. Phillion, R.C. Atwood, P.D. Lee, 4D synchrotron X-ray tomographic quantification of the transition from cellular to dendrite growth during directional solidification, Acta Mater. 117 (2016) 160–169. https://doi.org/10.1016/j.actamat.2016.07.002.
[26] B. Billia, N. Bergeon, H. Nguyen Thi, H. Jamgotchian, J. Gastaldi, G. Grange, Cumulative Mechanical Moments and Microstructure Deformation Induced by Growth Shape in Columnar Solidification, Phys. Rev. Lett. 93 (2004) 126105. https://doi.org/10.1103/PhysRevLett.93.126105.
[27] G. Reinhart, A. Buffet, H. Nguyen-Thi, B. Billia, H. Jung, N. Mangelinck-Noël, N. Bergeon, T. Schenk, J. Härtwig, J. Baruchel, In-Situ and Real-Time Analysis of the Formation of Strains and Microstructure Defects during Solidification of Al-3.5 Wt Pct Ni Alloys, Metall. Mater. Trans. A. 39 (2008) 865–874. https://doi.org/10.1007/s11661-007-9449-2.
[28] A. Buffet, H. Nguyen-Thi, A. Bogno, T. Schenk, N. Mangelinck-Noël, G. Reinhart, N. Bergeon, B. Billia, J. Baruchel, Measurement of Solute Profiles by Means of Synchrotron X-Ray Radiography during Directional Solidification of Al-4 wt% Cu Alloys, Mater. Sci. Forum. 649 (2010) 331–336. https://doi.org/10.4028/www.scientific.net/MSF.649.331.

[29] W.U. Mirihanage, K.V. Falch, I. Snigireva, A. Snigirev, Y.J. Li, L. Arnberg, R.H. Mathiesen, Retrieval of three-dimensional spatial information from fast in situ two-dimensional synchrotron radiography of solidification microstructure evolution, Acta Mater. 81 (2014) 241–247. https://doi.org/10.1016/j.actamat.2014.08.016.

[30] W.U. Mirihanage, K.V. Falch, D. Casari, S. McFadden, D.J. Browne, I. Snigireva, A. Snigirev, Y.J. Li, R.H. Mathiesen, Non-steady 3D dendrite tip growth under diffusive and weakly convective conditions, Materialia. 5 (2019) 100215. https://doi.org/10.1016/j.mtla.2019.100215.

[31] W.U. Mirihanage, L. Arnberg, R.H. Mathiesen, In-situ observation of transient columnar dendrite growth in the presence of thermo-solutal convection, IOP Conf. Ser. Mater. Sci. Eng. 33 (2012) 012033. https://doi.org/10.1088/1757-899X/33/1/012033.

[32] F. Cao, F. Yang, H. Kang, C. Zou, T. Xiao, W. Huang, T. Wang, Effect of traveling magnetic field on solute distribution and dendritic growth in unidirectionally solidifying Sn–50wt%Pb alloy: An in situ observation, J. Cryst. Growth. 450 (2016) 91–95. https://doi.org/10.1016/j.jcrysgro.2016.06.034.

[33] H. Yasuda, Y. Yamamoto, N. Nakatsuka, M. Yoshiya, T. Nagira, A. Sugiyama, I. Ohnaka, K. Uesugi, K. Umetani, *In situ* observation of solidification phenomena in Al–Cu and Fe–Si–Al alloys, Int. J. Cast Met. Res. 22 (2009) 15–21. https://doi.org/10.1179/136404609X368118.

[34] A. Tandjaoui, N. Mangelinck-Noel, G. Reinhart, B. Billia, T. Lafford, J. Baruchel, Investigation of grain boundary grooves at the solid–liquid interface during directional solidification of multi-crystalline silicon: in situ characterization by X-ray imaging, J. Cryst. Growth. 377 (2013) 203–211. https://doi.org/10.1016/j.jcrysgro.2013.05.023.

[35] J.W. Aveson, G. Reinhart, H. Nguyen-Thi, N. Mangelinck-Noël, A. Tandjaoui, B. Billia, K. Goodwin, T.A. Lafford, J. Baruchel, H.J. Stone, N. D'Souza, Dendrite Bending during Directional Solidification, in: E.S. Huron, R.C. Reed, rk C. Hardy, M.J. Mills, R.E. Montero, P.D. Portella, J. Telesman (Eds.), Superalloys 2012, John Wiley & Sons, Inc., 2012: pp. 615–624. http://onlinelibrary.wiley.com/doi/10.1002/9781118516430.ch69/summary (accessed March 31, 2014).

[36] J.W. Aveson, G. Reinhart, C.J.L. Goddard, H. Nguyen-Thi, N. Mangelinck-Noël, A. Tandjaoui, J.R. Davenport, N. Warnken, F. di Gioacchino, T.A. Lafford, N. D'Souza, B. Billia, H.J. Stone, On the Deformation of Dendrites During Directional Solidification of a Nickel-Based Superalloy, Metall. Mater. Trans. A. 50 (2019) 5234–5241. https://doi.org/10.1007/s11661-019-05429-0.

[37] M.A. Azeem, P.D. Lee, A.B. Phillion, S. Karagadde, P. Rockett, R.C. Atwood, L. Courtois, K.M. Rahman, D. Dye, Revealing dendritic pattern formation in Ni, Fe and Co alloys using synchrotron tomography, Acta Mater. 128 (2017) 241–248. https://doi.org/10.1016/j.actamat.2017.02.022.

[38] A. Tandjaoui, N. Mangelinck-Noël, G. Reinhart, J.-J. Furter, B. Billia, T. Lafford, J.

Baruchel, X. Guichard, Real Time Observation of the Directional Solidification of Multicrystalline Silicon: X-ray Imaging Characterization, Energy Procedia. 27 (2012) 82–87. https://doi.org/10.1016/j.egypro.2012.07.033.

[39] T. Riberi-Béridot, N. Mangelinck-Noël, A. Tandjaoui, G. Reinhart, B. Billia, T. Lafford, J. Baruchel, L. Barrallier, On the impact of twinning on the formation of the grain structure of multi-crystalline silicon for photovoltaic applications during directional solidification, J. Cryst. Growth. 418 (2015) 38–44. https://doi.org/10.1016/j.jcrysgro.2015.02.024.

[40] M.G. Tsoutsouva, T. Riberi – Béridot, G. Regula, G. Reinhart, J. Baruchel, F. Guittonneau, L. Barrallier, N. Mangelinck-Noël, In situ investigation of the structural defect generation and evolution during the directional solidification of 〈110〉 seeded growth Si, Acta Mater. 115 (2016) 210–223. https://doi.org/10.1016/j.actamat.2016.06.004.

[41] K. Harris, J.B. Wahl, Improved Single Crystal Superalloys, CMSX-4 (SLS)[La+Y] and CMSX-486, in: Superalloys 2004 Tenth Int. Symp., TMS, 2004: pp. 45–52. https://doi.org/10.7449/2004/Superalloys_2004_45_52.

[42] Thermo-Calc Software AB, NI25: Ni-based alloys and superalloy solutions database, (2007).

[43] Sente Software Ltd, JMatPro®, Www.Sentesoftware.Co.Uk. (n.d.).

[44] https://www.pco.de/scmos-cameras/pcoedge-55/, (2019).

[45] P. Cloetens, R. Barrett, J. Baruchel, J.-P. Guigay, M. Schlenker, Phase objects in synchrotron radiation hard x-ray imaging, J. Phys. Appl. Phys. 29 (1996) 133. https://doi.org/10.1088/0022-3727/29/1/023.

[46] M.D. Abramoff, P.J. Magalhães, S.J. Ram, Image processing with ImageJ, Biophotonics Int. 11 (2004) 36–42.

[47] P. Thévenaz, U.E. Ruttimann, M. Unser, A pyramid approach to subpixel registration based on intensity, IEEE Trans. Image Process. Publ. IEEE Signal Process. Soc. 7 (1998) 27–41. https://doi.org/10.1109/83.650848.

[48] H. Nguyen Thi, G. Reinhart, A. Buffet, T. Schenk, N. Mangelinck-Noël, H. Jung, N. Bergeon, B. Billia, J. Härtwig, J. Baruchel, In situ and real-time analysis of TGZM phenomena by synchrotron X-ray radiography, J. Cryst. Growth. 310 (2008) 2906–2914. https://doi.org/10.1016/j.jcrysgro.2008.01.041.

[49] H. Nguyen Thi, B. Drevet, J.M. Debierre, D. Camel, Y. Dabo, B. Billia, Preparation of the initial solid–liquid interface and melt in directional solidification, J. Cryst. Growth. 253 (2003) 539–548. https://doi.org/10.1016/S0022-0248(03)01041-8.

[50] A. Bogno, H. Nguyen-Thi, A. Buffet, G. Reinhart, B. Billia, N. Mangelinck-Noël, N. Bergeon, J. Baruchel, T. Schenk, Analysis by synchrotron X-ray radiography of convection effects on the dynamic evolution of the solid–liquid interface and on solute distribution during the initial transient of solidification, Acta Mater. 59 (2011) 4356–4365. https://doi.org/10.1016/j.actamat.2011.03.059.

[51] H.N. Thi, B. Billia, H. Jamgotchian, Influence of thermosolutal convection on the solidification front during upwards solidification, J. Fluid Mech. 204 (1989) 581–597. https://doi.org/10.1017/S0022112089001904.

[52] M.H. Burden, D.J. Hebditch, J.D. Hunt, Macroscopic stability of a planar, cellular or dendritic interface during directional freezing, J. Cryst. Growth. 20 (1973) 121–124. https://doi.org/10.1016/0022-0248(73)90125-5.

[53] G.K. Bouse, J.R. Mihalisin, 4 - Metallurgy of Investment Cast Superalloy Components, in: J.K. Tien, T. Caulfield (Eds.), Superalloys Supercompos. Superceram., Academic Press, 1989: pp. 99–148. https://doi.org/10.1016/B978-0-12-690845-9.50010-5.

[54] M.C. Schneider, J.P. Gu, C. Beckermann, W.J. Boettinger, U.R. Kattner, Modeling of micro- and macrosegregation and freckle formation in single-crystal nickel-base superalloy directional solidification, Metall. Mater. Trans. A. 28 (1997) 1517–1531. https://doi.org/10.1007/s11661-997-0214-3.

[55] G. Matache, D.M. Stefanescu, C. Puscasu, E. Alexandrescu, Dendritic segregation and arm spacing in directionally solidified CMSX-4 superalloy, Int. J. Cast Met. Res. 29 (2016) 303–316. https://doi.org/10.1080/13640461.2016.1166726.

[56] D. Tourret, A. Karma, A.J. Clarke, P.J. Gibbs, S.D. Imhoff, Three-dimensional Dendritic Needle Network model with application to Al-Cu directional solidification experiments, IOP Conf. Ser. Mater. Sci. Eng. 84 (2015) 012082. https://doi.org/10.1088/1757-899X/84/1/012082.

[57] A.J. Clarke, D. Tourret, Y. Song, S.D. Imhoff, P.J. Gibbs, J.W. Gibbs, K. Fezzaa, A. Karma, Microstructure selection in thin-sample directional solidification of an Al-Cu alloy: In situ X-ray imaging and phase-field simulations, Acta Mater. 129 (2017) 203–216. https://doi.org/10.1016/j.actamat.2017.02.047.

[58] C. Yang, Q. Xu, B. Liu, Study of dendrite growth with natural convection in superalloy directional solidification via a multiphase-field-lattice Boltzmann model, Comput. Mater. Sci. 158 (2019) 130–139. https://doi.org/10.1016/j.commatsci.2018.11.024.

[59] J.A. Warren, J.S. Langer, Prediction of dendritic spacings in a directional-solidification experiment, Phys. Rev. E. 47 (1993) 2702–2712. https://doi.org/10.1103/PhysRevE.47.2702.

Captions

Element	Cr	Co	W	Al	Mo	Re	Ti	Hf	Ta	Ni
Composition (wt.%)	6.5	9.6	6.4	5.6	0.6	3	1	0.1	6.5	Balance

Table 1 Nominal composition of the CMSX4 Ni-based superalloy.

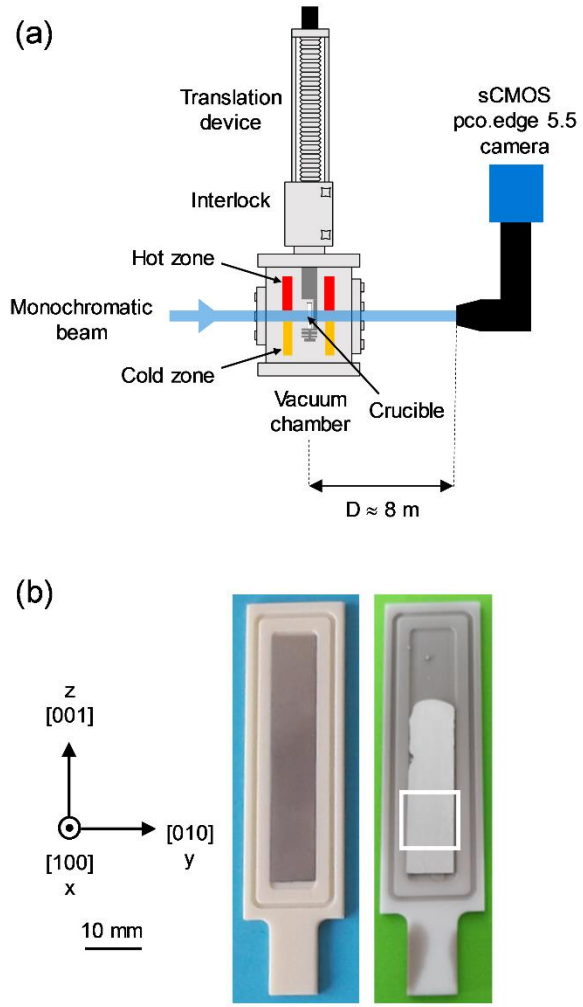

Fig. 1. (a) Schematic drawing of the experimental device used to carry out X-ray imaging at the ID19 beamline of ESRF during directional solidification at high temperature. (b) Pictures of the CMSX-4 sample with its crucible before (left) and after (right) the melting-solidification sequences. The white square in the right-hand-side picture represents the field of view of the present experiment.

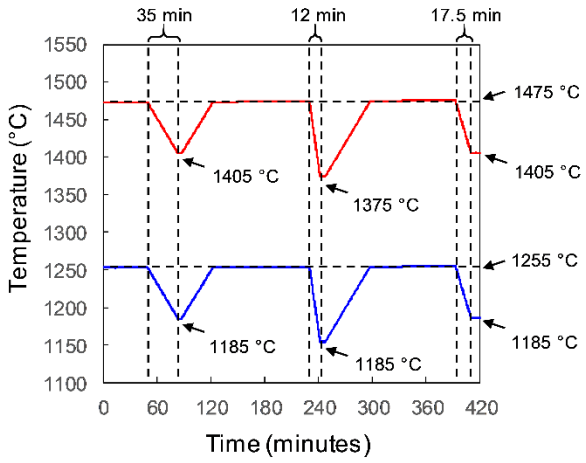

Fig. 2. Experimental temperature profiles recorded during the experiments and showing the successive cooling, stabilization and heating steps.

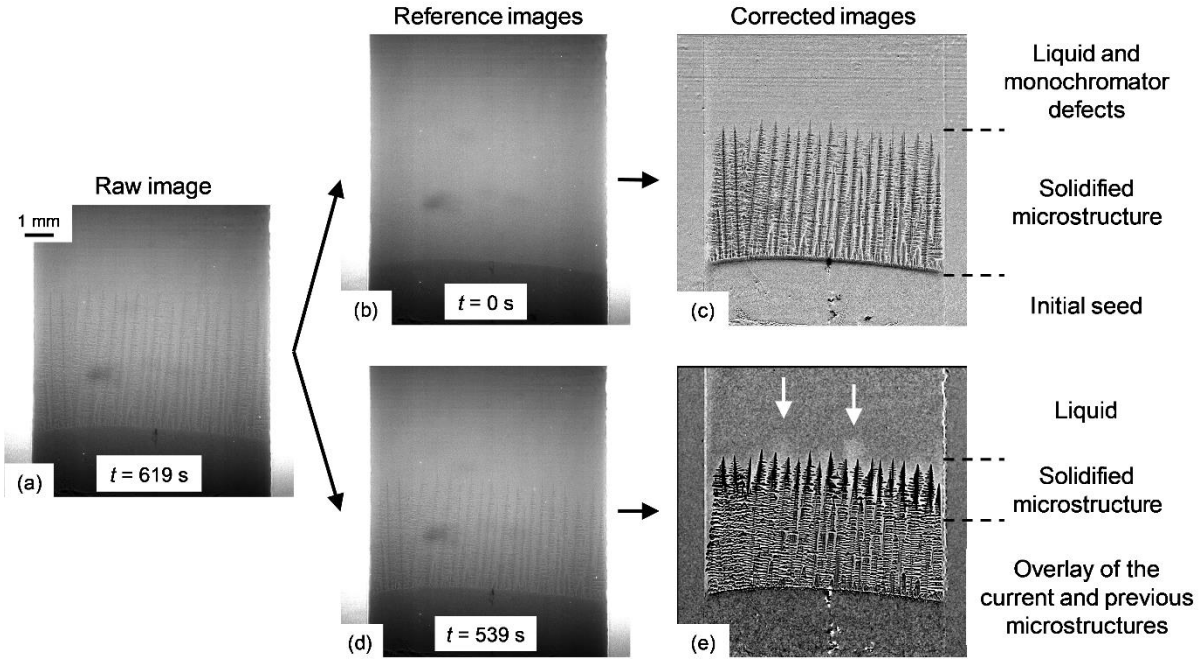

Fig. 3. Illustration of the two image processing procedures used to improve the legibility of the images. (a) Raw image, (b) reference image recorded before applying the cooling rate, (c) result of the flat-field correction revealing more clearly the growth microstructure, (d) reference image recorded at a previous time and (e) result of the frame differencing procedure showing gray-level variations in the liquid phase due to solute rejection. (R = –2 °C·min^{-1}, G_F = 44 °C·cm^{-1})

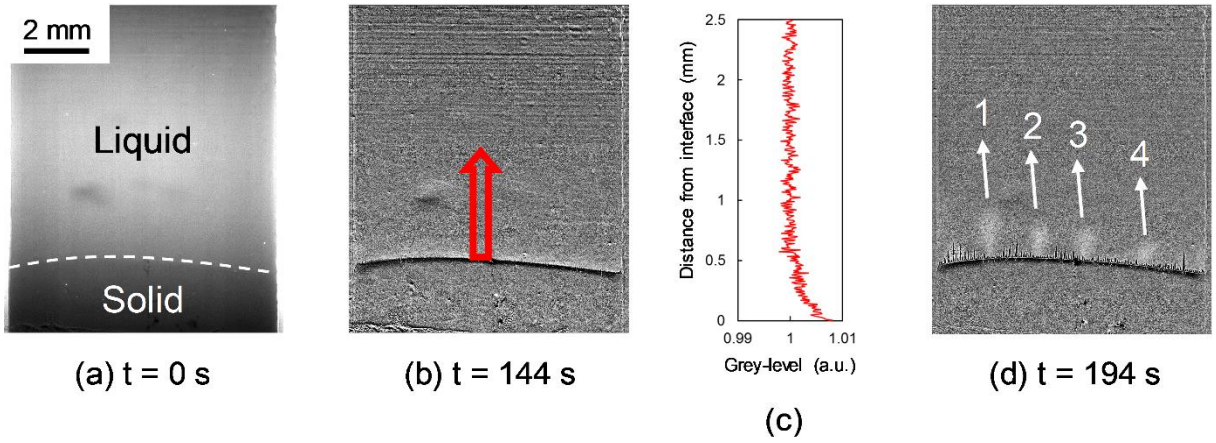

Fig. 4. Time sequence of the initial transient showing the solid-liquid interface destabilization. (a) Raw image with the initial solid-liquid interface in the field of view highlighted by a dashed line. (b) Image recorded before destabilization and obtained by flat-field correction : the solid that was formed appears in dark gray and the solutal layer above the solidification front is visible as a light gray layer and is better revealed by (c) the gray-level profile measured in the region corresponding to the red arrow in (b). (d) Formation of solute plumes indicated by four white arrows after destabilization of the solutal layer. (R = –2 °C·min^{-1}, G_F = 44 °C·cm^{-1}).

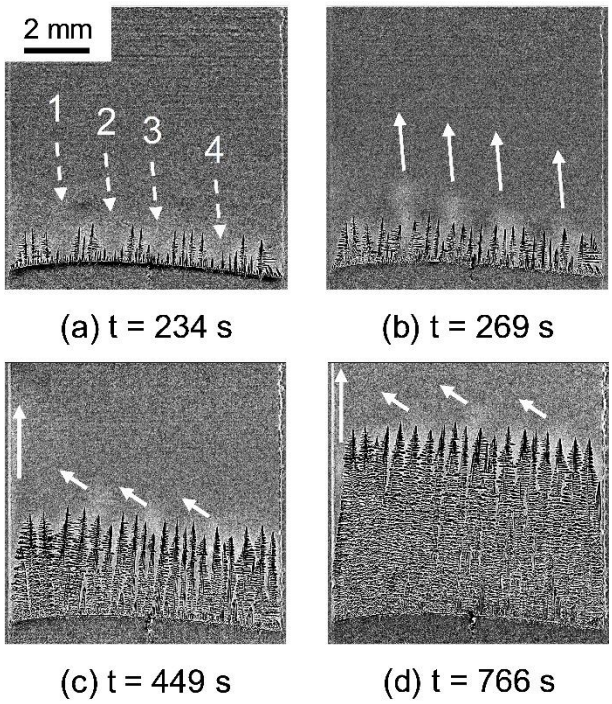

Fig. 5. Time sequence showing (a) the development of columnar dendritic structures after destabilization of the solid-liquid interface and (b) the formation of solute plumes above growing dendrites. The dashed arrows indicate the position of the previous solute plumes visible in Fig. 3d. Upon solidification of the network of columnar dendrites (c) and (d) the solutal convective flow propagates in the directions given by the white arrows. (R = –2 °C·min^{-1}, G_F = 44 °C·cm^{-1}, frame differencing).

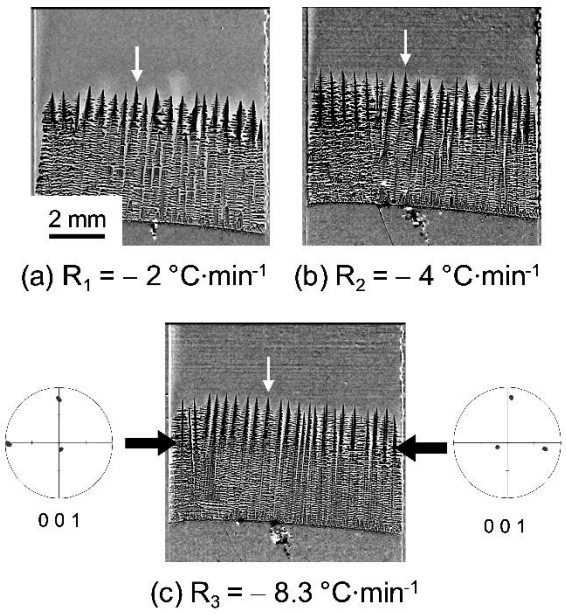

Fig. 6. Images of the growing dendritic microstructure for the three studied cooling rates (frame differencing). The white arrows indicate the dendrites whose positions and growth velocities are measured in Fig. 6.

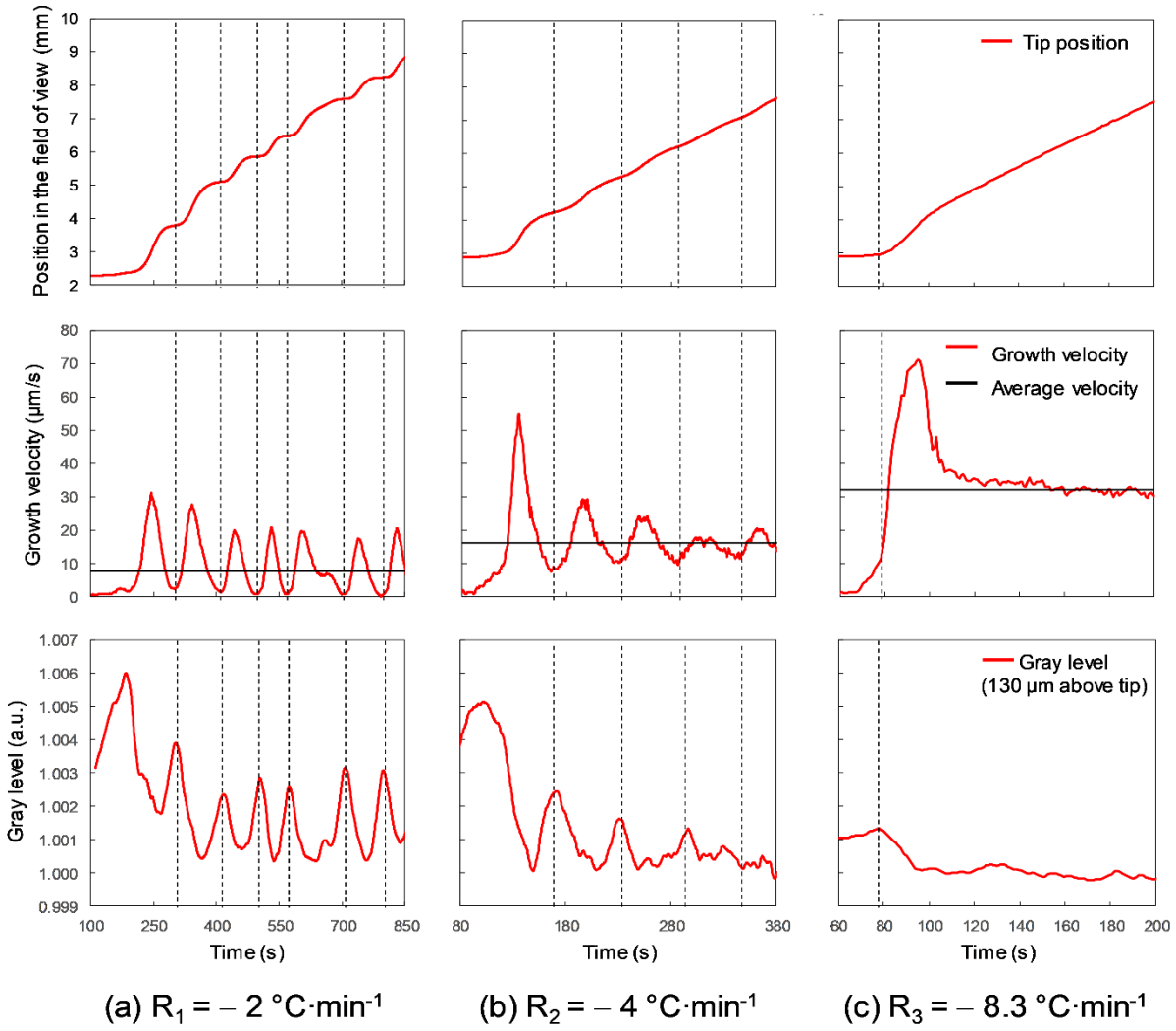

Fig. 7. Time evolution of the tip position in the field of view (top row), the growth velocity (middle row) and the average gray level (bottom row) in a 130×130 µm^2 box with its center located 130 µm above the dendrite tips shown in Fig. 5. The error bars of the position (± 6.6 µm) and velocity (± 0.6 µm/s) values are smaller than the line thickness. The black horizontal lines in the growth velocity plots correspond to the average velocities and are (a) 7.6 µm/s, (b) 15 µm/s and (c) 31 µm/s for the cooling rates of (a) –2 °C/min, (b) –4 °C/min and (c) –8.3 °C/min.

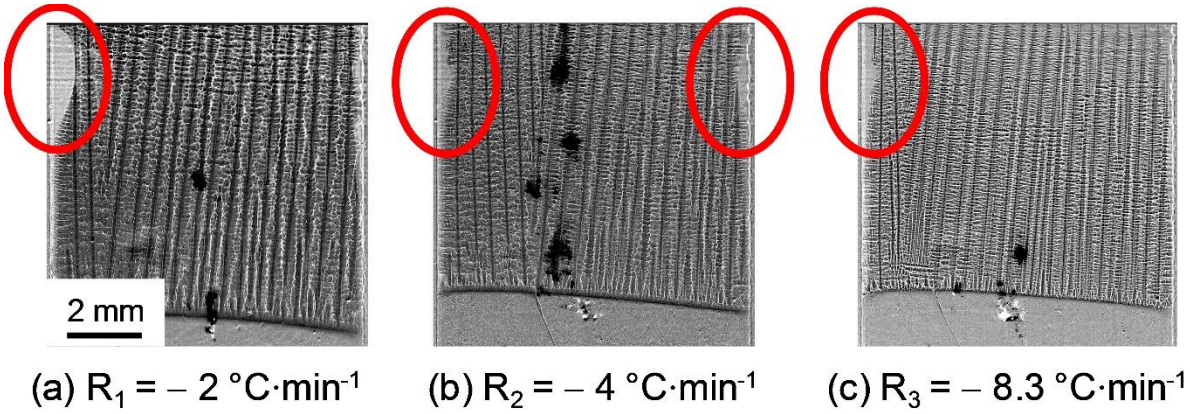

Fig. 8. Images showing regions where residual liquid areas were formed after the solidification front left the field of view (red ellipses). The black areas in the microstructure correspond to dendrite parts that are in Bragg position for the monochromatic beam energy: these areas locally diffract the direct X-ray beam and thus no intensity is recorded on the radiographs.

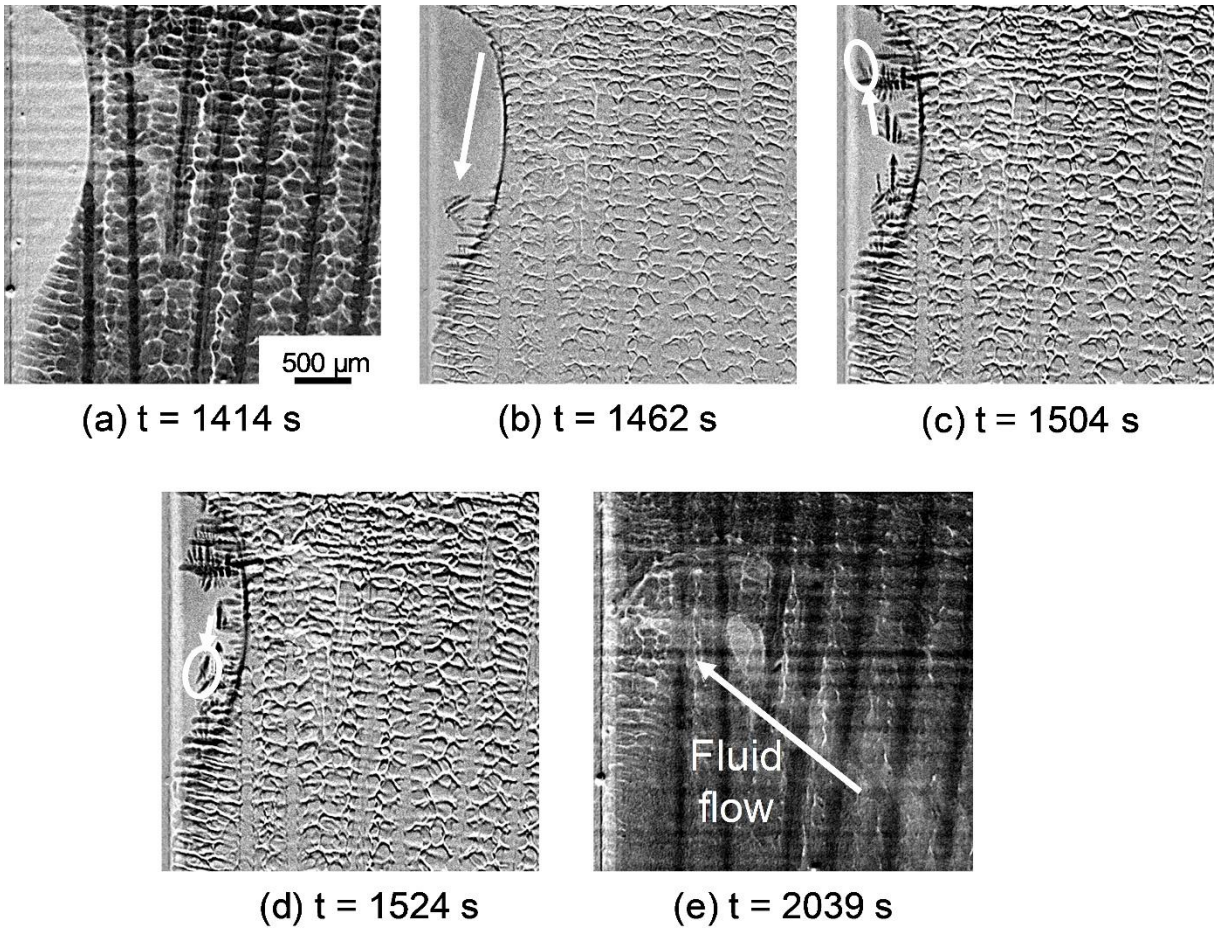

Fig. 9. Sequence of close-ups showing the solidification of a residual liquid area on the side of the sample starting from (a) the time when it reached its largest size. The white arrows in (b) and (d) indicate the trajectory of dendrite fragments that settled down in the residual liquid area (frame differencing) while the white arrow in (c) indicates the trajectory of a dendrite fragment that was transported upward in the residual liquid area (frame differencing). An image recorded when the sample was fully solidified is shown in (e). The top-left to bottom-right light gray area corresponds to a region where the microstructure was dissolved, possibly due to convective flow that developed in the mushy zone and transporting solute rich liquid, leading to local segregation. (R = –2 °C·min^{-1}, G_F = 44 °C·cm^{-1})

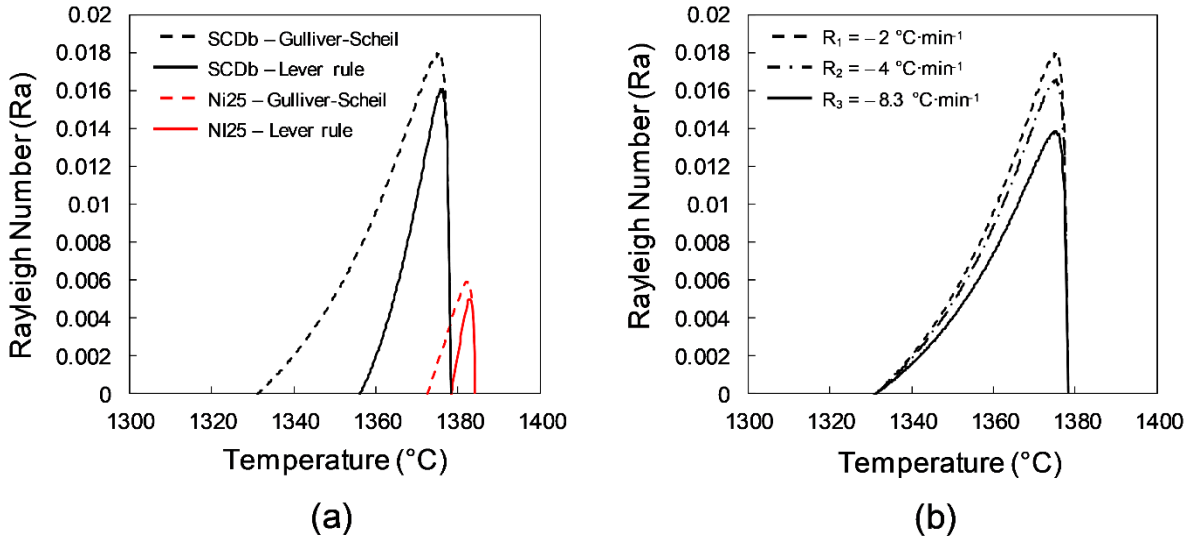

Fig. 10. Variations of Rayleigh number (a) as a function of the temperature for different databases and micro-segregation models (R = –2 °C·min^{-1}). (b) Variations of Rayleigh number for different cooling rates using the Single Cristal database (SCDb) and Gulliver-Scheil model.